



HAL
open science

Recyclable metal fuels as future zero-carbon energy carrier

Fabien Halter, Samuel Jeanjean, Christian Chauveau, Youssef Berro, Marianne Balat-Pichelin, Jean-François Brillhac, Adeline Andrieu, Cornelius Schonnenbeck, Gontrand Leyssens, Clément Dumand

► **To cite this version:**

Fabien Halter, Samuel Jeanjean, Christian Chauveau, Youssef Berro, Marianne Balat-Pichelin, et al.. Recyclable metal fuels as future zero-carbon energy carrier. *Applications in Energy and Combustion Science*, 2023, 13, pp.100100. 10.1016/j.jaecs.2022.100100 . hal-03875164

HAL Id: hal-03875164

<https://hal.science/hal-03875164>

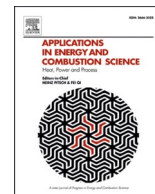
Submitted on 7 Apr 2023

HAL is a multi-disciplinary open access archive for the deposit and dissemination of scientific research documents, whether they are published or not. The documents may come from teaching and research institutions in France or abroad, or from public or private research centers.

L'archive ouverte pluridisciplinaire **HAL**, est destinée au dépôt et à la diffusion de documents scientifiques de niveau recherche, publiés ou non, émanant des établissements d'enseignement et de recherche français ou étrangers, des laboratoires publics ou privés.



Distributed under a Creative Commons Attribution - NonCommercial - NoDerivatives 4.0 International License



Recyclable metal fuels as future zero-carbon energy carrier

F. Halter^{a,b,*}, S. Jeanjean^{a,b}, C. Chauveau^a, Y. Berro^c, M. Balat-Pichelin^c, J.F. Brilhac^d,
A. Andrieu^d, C. Schonnenbeck^d, G. Leyssens^d, C. Dumand^e

^a CNRS ICARE, Avenue de la Recherche Scientifique, 45071 Orléans Cedex 2, France

^b Université d'Orléans, Orléans, France

^c PROMES-CNRS, 7 rue du four solaire, 66120 Font-Romeu Odeillo, France

^d LGRE UR 2334, Université de Haute-Alsace 68093 Mulhouse Cedex, France

^e STELLANTIS Research, Innovation & Advanced Technologies Science for Energy, Powertrain & Converter Rte de Gisy, 78140 Vélizy-Villacoublay

ARTICLE INFO

Keywords:

Zero-carbon energy carrier
Metal particles
Carbothermal reduction
Direct combustion
Aluminum
Magnesium
Solar energy

ABSTRACT

What if small metal particles were the future of energy?

Combustion of these metal particles releases a large amount of energy and has the advantage of not emitting carbon dioxide. These particles, burning in air, produce metal oxides which can then be regenerated using solar energy. This cycle energy production / recycling can make it possible to store energy produced with renewable energy in a secure and sustainable way, so that it can be used where and when it is needed.

The STELLAR project described in this paper, funded by the French research agency, allows a group of research and industrial partners to work on this original and promising concept. This work is part of a disruptive technology to solve the problem of global warming in the long term.

1. Introduction and presentation of the concept

1.1. Zero-Carbon fuels

Limiting global warming to 1,5 °C is the common goal of the worldwide economies. On this basis, Europe has launched its Green Deal, and the European Commission has proposed its Fit for 55 Program [1] reducing the tank to wheel CO₂ emissions from transport by 55% in 2030, and by 100% in 2035 which will then ban all powertrains with CO₂ emissions.

Big car companies are moving forward to decarbonation. As an example, Stellantis, a multinational automotive manufacturing corporation (merger between the conglomerate Fiat Chrysler Automobile and the French PSA Group), is committed to become a carbon neutral stakeholder by the end of 2038. This commitment concerns all the Stellantis activities and products.

Meeting such Tank to Wheel (TtW) emissions requires carbon free energy carriers for all type of mobile applications with the constraints to always cover sufficient range, to have a guaranteed available energy distribution network and to maintain cost and complexity as low as possible.

To answer both global scale and carbon dioxide emissions issues,

hydrogen and its derivate may be seen as a possible candidate to store overproduction from renewables. As illustrated in Fig. 1, hydrogen, produced from green electricity through water electrolysis, is the keystone in the production of two fuels families: zero carbon fuels (hydrogen and ammonia) and drop in fuels (Gasoline, Kerosene, Diesel). All of them are called eFuels. eFuels are produced with the help of electricity from renewable energy sources, water and CO₂ from the air. In contrast to conventional fuels, they do not release additional CO₂ and are climate neutral in the entire balance. Thanks to their compatibility with today's technologies, eFuels can power vehicles, airplanes and ships, thus allowing them to continue to operate but in a climate-friendly manner. The same applies to all heating systems that use liquid and gaseous fuels. Existing transport, distribution and fuel/gas infrastructures can also continue to be used.

Similarly, and mainly due to storage and distribution complexities related to hydrogen, micrometric metal particles could be a better option especially for long-term energy storage.

Metal particles show a very good energy density, similar to liquid hydrocarbons, enabling, in a transportation context, a much higher autonomy than a pure electric vehicle, even at long-term and can be used as a range extender solution with an external combustion engine. The high energy density inherent to reactive metals, which motivates

* Corresponding author at: 1C Avenue de la Recherche Scientifique, 45067 ORLEANS Cedex 2, France.

E-mail address: fabien.halter@univ-orleans.fr (F. Halter).

their use as additives to propellants and energetic materials, or as anodes within batteries, also inspires their use as recyclable solar fuels.

The possibility to use metal powder to store energy from intermittent renewable energy sources arises naturally as a close to zero GHG emission well-to-wheel specific reduction process can be performed from the oxidized metal particulates using concentrated solar energy.

1.2. Metal particles as an energy carrier

Under the impetus of McGill’s research group, the use of metallic particles as an energy carrier is experiencing growing interest. Many research and industrial groups have initiated studies in this field and the reader is referred to the comprehensive review by Berghthorson [2].

Micron-sized metal powders are easily transportable, are safer and more stable to handle than nano particles or gaseous fuels. They have a practically unlimited shelf life when protected from humidity in hermetically-sealed containers. The energy consumption for producing industrial powders in the micron-size range is close to the energy intensity of the primary metal production [3], suggesting that they will have much lower costs and better energy-cycle efficiency compared to metal-air batteries, which require expensive high-purity anodes, or metal-fuel combustors/reactors burning expensive nano-powders.

Metal particles seem difficult to apply in a current internal combustion engine but compliant with an external combustion engine, more likely to be used as a steady power source as requested for a range extender in road transport, a drone, or an auxiliary power unit for aviation. Even when compared to a very optimistic Li-ion cells density of 1 MJ/kg, the estimated autonomy would still be more than quadruple. Compared to most promising H₂ fuel cells, this vector is expected to be safer for the on-board storage and to rely on a simpler distribution infrastructure.

In a concept of metal-fuel economy, metals, typically as powders, are burned with air to produce heat for a heat engine. Metal fuels produce metal oxides, which are typically solid under standard conditions and can be collected for recycling. Metal fuels can be recycled from the metal oxide products, using clean primary energy sources, an effectively infinite number of times while avoiding loss of material to the environment. Preliminary life cycle and economic assessments have been performed for some potential metal fuels [4], with the results generally indicating that metal fuels can be competitive options to either metal-air

batteries or hydrogen on the basis of their costs and energy-cycle efficiency. Due to the oxidation of the metal powders from oxygen in the air, the global weight of the system increases during the process. This is not a concern for stationary applications but does reduce the performance of metal fuels for transportation systems.

Out of all of the metals identified as possible energy carriers, silicon, aluminum, iron and magnesium are the 2nd, 3rd, 4th and 6th most abundant elements in the Earth’s crust, respectively; the most abundant element being oxygen, typically in the form of an oxide of these metals. Iron is, by far, the most used metal today and is a promising solar fuel. Silicon, technically a metalloid rather than a metal, is another potential energy carrier, since it can be produced from sand (SiO₂), water, and solar energy [5]. Aluminum and magnesium are very interesting as metal fuels due to their high energy density, relatively low costs, and the potential to recycle them with low carbon emissions. Aluminum has already been studied for decades in pyrotechnic and solid propellants. It is easy to transport and store. When it is placed into the atmosphere, it is covered by oxide film, which protects metal from further corrosion, thus providing the safety of its storage and transportation. Magnesium is less exploited by the industry compared to iron and aluminum. It has a lower melting point (650 °C) and vaporization temperature (1090 °C) than aluminum. This feature is an advantage when developing a new combustion system as the turbulent swirled burner.

Table 1 shows the initial metal mass and the final oxides generated mass we target for a typical autonomy of 750 km in pure thermal mode. The average mass of Diesel needed to cover an equivalent distance has also been added. In this case, final mass is zero.

The enthalpies of the Metal combustion reaction ($Metal + Oxidizer \xrightarrow{yields} Metal\ oxide$) provide a measure of their chemical energetic potential when used as a fuel in combination with ambient oxygen [4, 6-9]. Fig. 2 indicates promising energetic content for three different metals (Al, Mg, Fe), making them relevant for transportation

Table 1
Metal and oxide masses for 750 km autonomy.

(kg)	Al	Mg	Fe	Diesel
Initial Mass	53	72	144	39
Final Mass	100	119	206	-

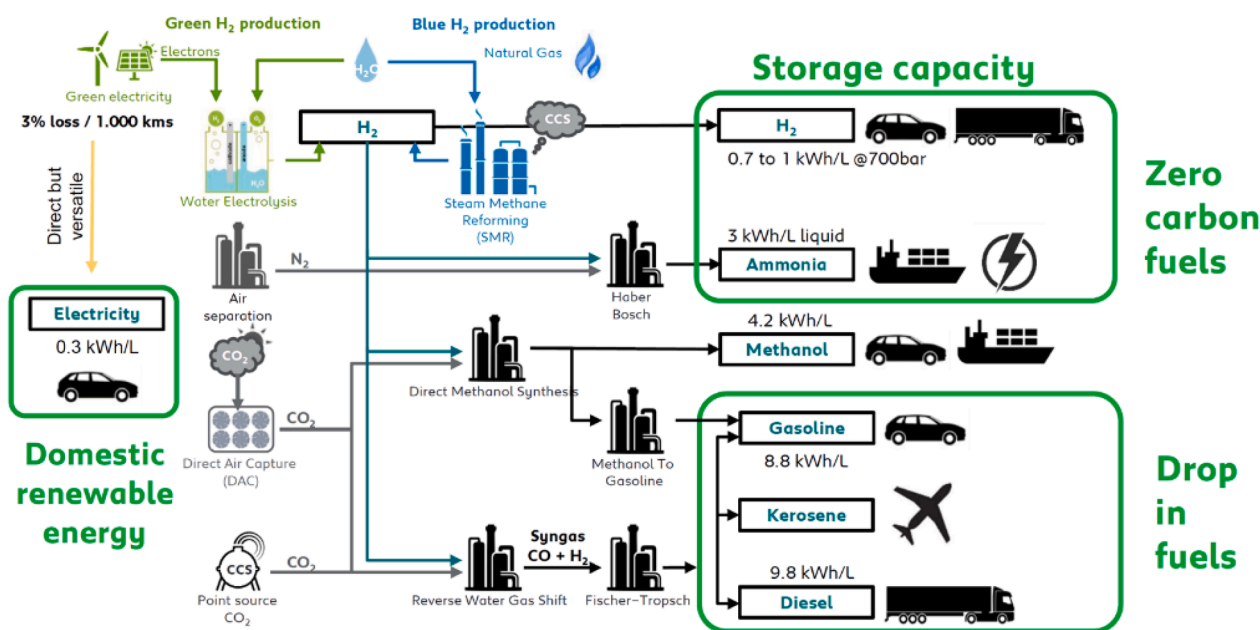


Fig. 1. Illustration of e-fuel production.

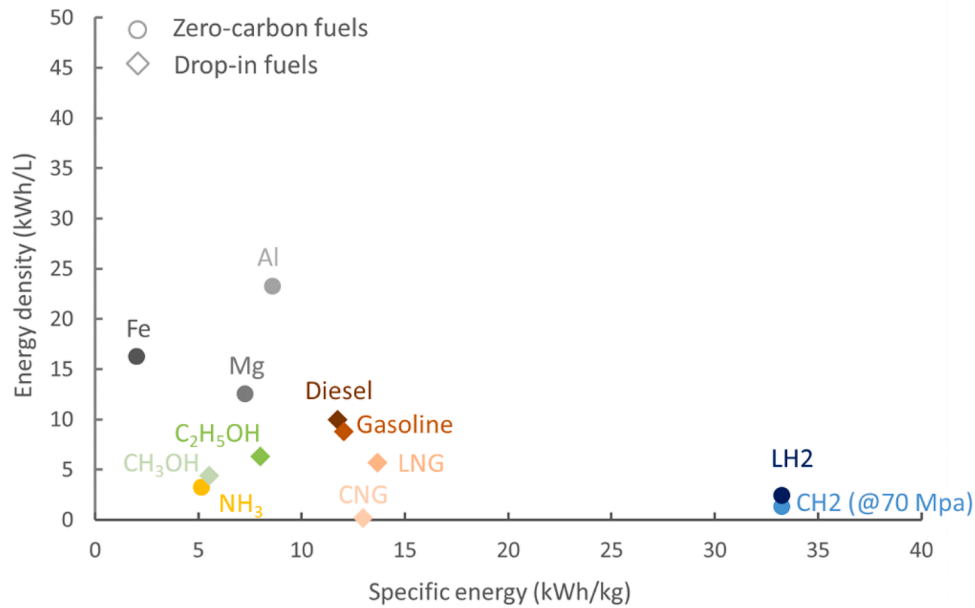


Fig. 2. Metal and efuels combustion enthalpies.

purpose. Their specific energy and energy density are compared to previously mentioned zero carbon fuels (circles) and Drop-in fuels (diamonds).

Energy density values are displayed as this is what first caught attention. This is, of course, a potential. But as this potential is high, we can reasonably imagine that the global system is virtuous. However, the objective of the paper is to show the potential more than to carry out a complete comparison on different propulsion systems. It is premature to be able to compare the systems in their entirety given that the technology using metallic particles is not mature enough for the moment. Systems will have to be judged with a multi-criteria approach. There is the size of the system in the vehicle, the autonomy, the recharge time, the cost, the overall environmental footprint, the dependence on rare metals, etc. There is probably no single solution. The system we are studying is similar to a battery electric vehicle (BEV) because in both cases the car will be propelled by an electric traction chain. BEVs are suitable for urban vehicles with small batteries. The combustion of metal powders may one day provide a solution for long-range vehicles with a fast-charging solution using carbon-free energy.

The proposed project focuses on the transportation sector, which leads us to favor the study of aluminum and magnesium. Nevertheless, the technological advances achieved can be extrapolated to other less energetic solid fuels promising for energy storage.

The possibility to use metal powder to store energy from intermittent renewable energy sources naturally arises. Since metals are not available in pure reduced form in the Earth's crust, they need to be produced from their oxides (ores or discarded metallurgical by-products). Unlike hydrocarbons, the energetic content will be introduced by the reduction process of the material itself. Thus, to keep the well-to-wheel GHG emission levels close to zero, this oxide reduction occurring after combustion of metal particles will be done in a separate process and location using concentrated solar power (CSP). The concept of a zero-emission vehicle is illustrated in Fig. 3. The heat released by the stationary metal particles combustion is valorized thanks to an external combustion engine to produce mechanical energy which is ultimately transformed into electricity. Produced metal oxides are filtered and kept on board in a separate tank to be recycled afterwards using solar energy in a dedicated recycling unit. This process involves no rare earth materials or

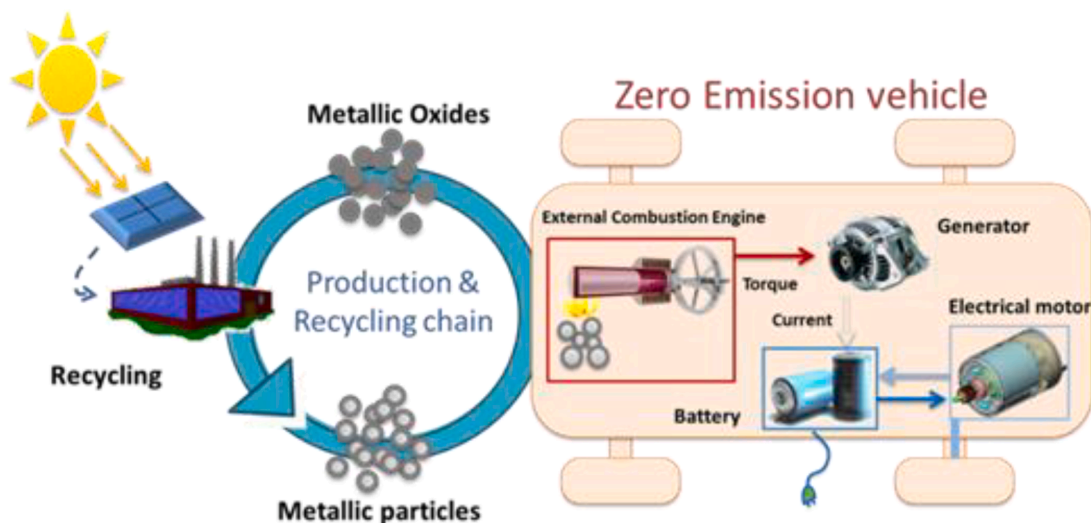


Fig. 3. Illustration of the Metal oxidation/reduction cycle.

expensive technology that could affect the usual cost fade linked to mass production.

It should also be underlined that no negative impact on raw material resources is expected to arise as the deployment of this technology would be based on a closed cycle using resources abundant enough to feed the initial working capital.

The global objective of this paper is to provide a clear assessment of the potential of metal particles as fuels for mobility. More specifically, this study provides new information on the following points: the stabilization of a confined turbulent flame, the composition and morphology of the particles produced, the ability of commercial systems to filter these particles, the ability of solar carbon reduction to regenerate the particles. This study is the first, to our knowledge, to couple heat production and recycling. Both the oxidation and reduction processes will be detailed and discussed. Two different experimental set-ups were developed to study the combustion process. Each of them was devoted to a different metal (Magnesium in LGRE-UHA and Aluminum in ICARE). The work done in LGRE-UHA mainly focuses on the solid and gas-phase products characterization. Both studies proposed an energy balance and the combustion process was scrutinized in ICARE. The reduction process described in the last part was performed in PROMES.

2. Direct combustion of metal particles with air

2.1. General introduction

Metal particles selected in the project (i.e. Mg & Al) burn with air at ambient conditions in a vapor-phase regime [2]. The process encountered by each individual particle is illustrated in Fig. 4. Part of the heat produced in the reaction zone diffuses back to the particle (yellow arrow) and allows the metal vaporization. Surrounding oxygen also diffuses to the reaction zone. The combustion occurs in the vapor phase and produces metal oxides which instantaneously condense if the local temperature is lower than its dissociation or vaporization temperature. Some melted metal oxide lobe remains on the metal particle surface. This oxide comes from the initial oxide layer naturally covering the raw material. More details of the combustion process may be found in [10–13].

The combustion of aluminum has been widely studied over the past decades including ignition, burning time and group combustion. In particular, the reader is referred to the work of Soo et al. [14] where ignition and combustion of single particles, agglomerates and suspensions are reviewed and analyzed. Many investigations consider magnesium combustion under different atmospheres, among which are carbon dioxide at low pressure [15], water vapor [16] and O₂-inert atmosphere [17]. Fundamental researches on burning processes and mechanisms are

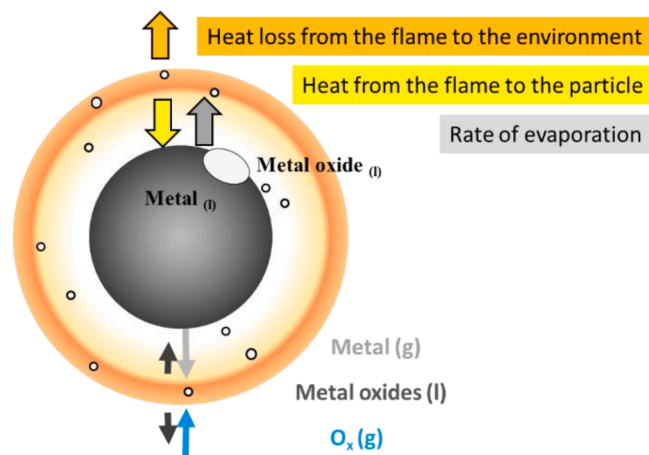


Fig. 4. Illustration of the Aluminum particle combustion in the vapor-phase regime.

also widely referenced [18,19]. The ignition and burning of metal particles are also well documented [3,20,21]. The micron-sized metal particles or nano-sized particles [8] exhibit shorter burning times.

The gaseous pollutants resulting from the metal combustion in air are nitrogen oxides. During the combustion of magnesium or aluminum, the 2000 °C hot flame generates high levels of thermal NO_x emissions [22]. These NO_x levels must therefore be reduced drastically. The rates of NO_x production depend on several factors, such as the temperature of the flame but also the availability of oxygen in the flame and consequently the local equivalence ratio. This will be detailed later in the paper.

The resulting metal oxides are nanometric or micrometric particles [9,23]. The metal oxide trapping efficiency must be as close as possible to 100% for an efficient fuel lifecycle first. Additionally, particle emission is one of the major issues of all the available combustion systems even with a clean and renewable fuel. This is why the investigation of particles trapping and emission from metal fuel combustion is essential.

The combustion process as well as the gaseous and condensed products have been scrutinized using two complementary experimental set-ups which are described below.

2.2. Burner in LGRE-UHA (Magnesium)

2.2.1. Description of the device

The metal-air burner [23] developed at LGRE-UHA is depicted in Fig. 5. This innovative power device has been designed for heat generation and recovering through magnesium combustion. It is composed of three main parts: an air and magnesium injection, a combustion chamber with an optical access for the flame observation, two consecutive cyclones to collect the MgO particles and a secondary heat exchanger.

The combustion chamber consists in a cooled double-walled pipe, 0.6 m long with an internal diameter of 0.105 m. The heated gas and magnesium oxides particles are driven through a convergent to the tangential entry of a first cyclone. A second cyclone improves magnesium oxide trapping. Then the hot gas flows to the secondary heat exchanger.

The metal fuel is a magnesium powder with a purity greater than 99.8% and supplied by Carl Roth as CP20.2 reference. Three size ranges are investigated: as received, 20 to 50 μm, 50 to 70 μm. Solid fuel injection was conducted with a PALAS BEG 1000 type B which allows a continuous and homogeneous injection of particles. The injected airflow rate ranges between 4.6 Nm³.h⁻¹ and 8.6 Nm³.h⁻¹. The oxygen concentration at the outlet of the system is monitored using a paramagnetic X Stream Rosemount O₂ analyser. Global equivalence ratio is estimated from the O₂ mole fractions measured at the device's outflow. It varies from 0.14 to 1.2 by increasing the flow of the magnesium injected at constant air supply injection. For such a range of equivalence ratio and depending on the dilution, the power supplied by the combustion varies between 6 and 23 kW. Heat recovery is achieved with the water-cooled combustion chamber and with the secondary heat exchanger. More than 70% of the power dissipated by the combustion is recovered [23].

The gas temperature profile in the combustion chamber is characterized using a set of type K thermocouples located along the chamber axis (see Fig. 5). Additionally, the temperature of particles in the flame are measured using an IMPAC infrared ISR 12-LO bichromatic pyrometer ($\lambda_1=800$ nm, $\lambda_2=1050$ nm).

2.2.2. Stabilization of the swirled flame

The magnesium flame is stabilized by a swirled flow which is generated by a secondary air injected through four tangential inlets in the injection head as shown in Fig. 5. Swirl stabilization allows a flame holding with a high power dissipated in a small sized burner. The geometric swirl number S_g [24] is a function of the ratio between axial mass flow rate and tangential mass flow rate and two swirl conditions are investigated: $S_g = 0.7$ (low swirl) and $S_g = 7.3$ (high swirl).

The lower limit of the flame stability is obtained for an equivalence ratio equal to 0.2 with the high swirl. For lower equivalence ratios, the

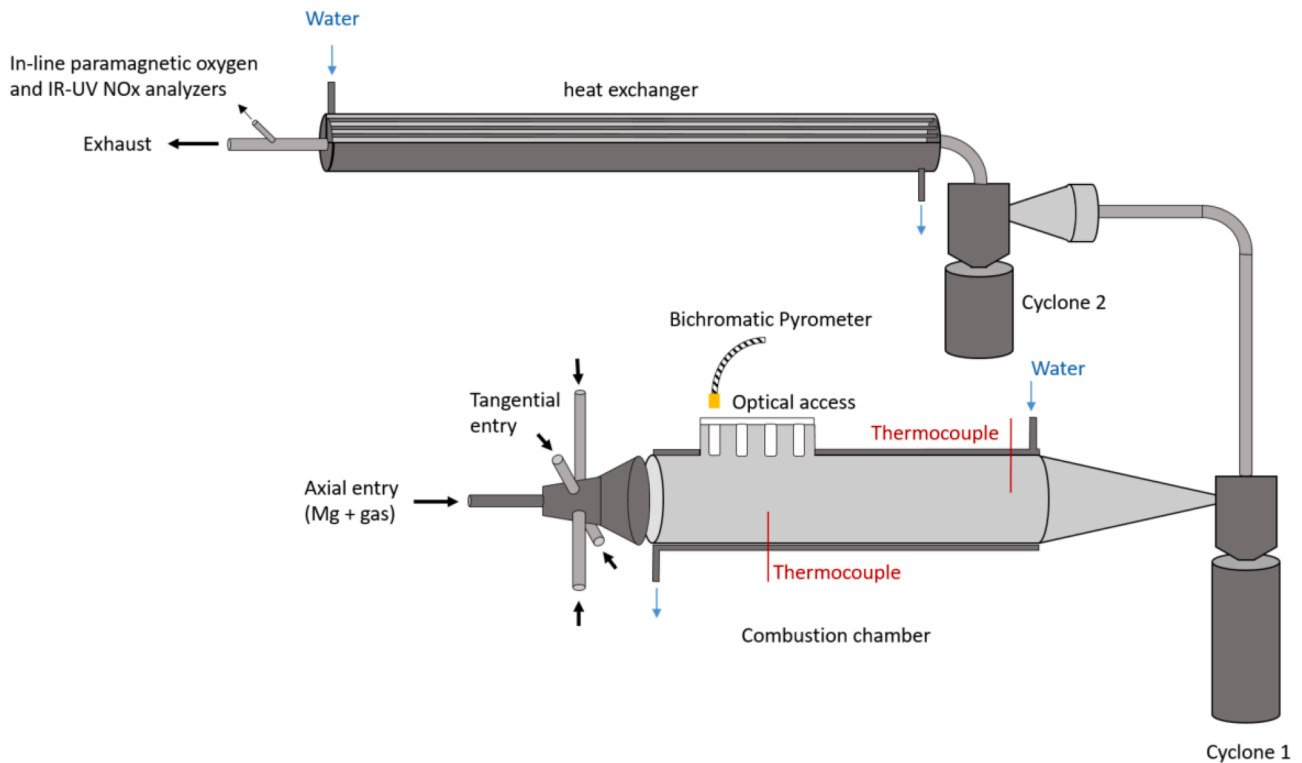


Fig. 5. Scheme of the magnesium-air burner. Adapted from [23].

power dissipated by the combustion is not sufficient to maintain the self-sustainable flame [25]. The flame stability is not affected by the particle size range.

2.2.3. Strategies to reduce NOx emissions

It is necessary to overcome the possible issue with NOx production considering the high temperatures of a metal flame. Previously, the influence of swirl on NOx emissions has been studied [25] and Fig. 6 describes the results obtained with 0% dilution for two levels of swirl. An Exhaust Gas Recirculation (EGR) is an appropriate strategy for NOx reduction [26] with the metal-air burner. Nitrogen is injected in the carrier gas (between 0 and 4.3 Nm³.h⁻¹) to mimic EGR. The dilution

with nitrogen is done without any modification of the volume of the carrier gas. Air and nitrogen are mixed together before being injected in the axial and tangential gas inlet. The air/nitrogen mixtures allow obtaining dilution ratios of 0% and 50% nitrogen, the dilution rates being expressed as a volume percentage. For these experimental conditions, the chamber opens onto a long outlet pipe instead of the cyclones and exchanger. A sample of the outlet gas flow is collected using a tube with three bored holes which are positioned perpendicularly to the flow. The NO and NO₂ emissions are monitored using infrared and ultraviolet cells of X Stream Rosemount analysers. N₂O, a major scavenger of stratospheric ozone, will be measured in a future work. NOx are measured in ppm and are also expressed in g.kW⁻¹.h⁻¹ relating to the

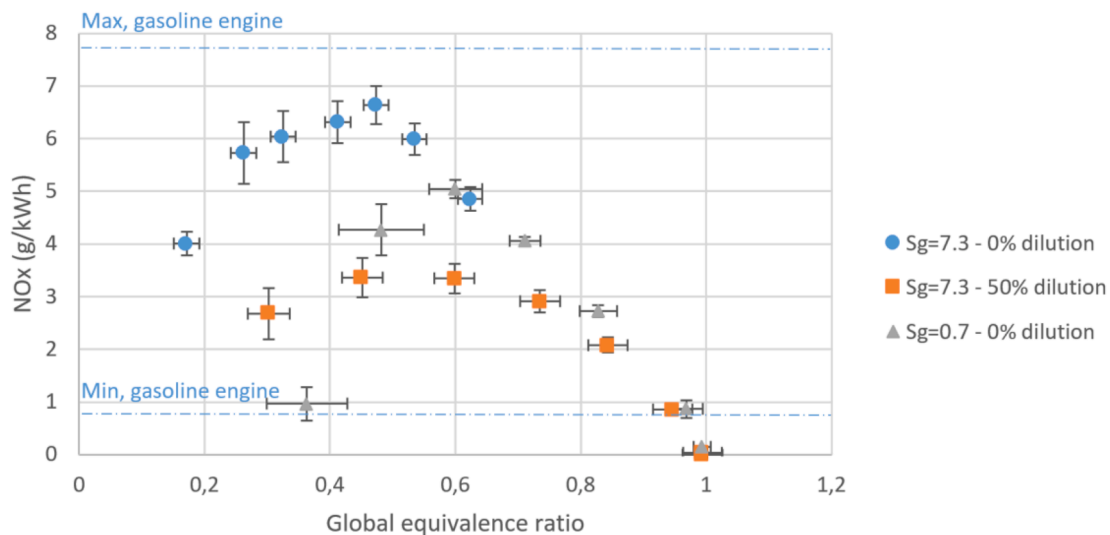


Fig. 6. NOx emission versus global equivalence ratio. Comparison with the regulated NOx emissions of a gasoline engine.

power dissipated by the combustion for comparison with NO_x emission from gasoline engines.

Figure 6 depicts the NO_x mole fractions as a function of the global equivalence ratio. It exhibits a curve with a maximum for an equivalence ratio around 0.5. Whatever the experimental conditions, the amount of NO formed is four times greater than the amount of NO₂ formed. With a 50% dilution, the amount of NO_x formed is halved and the amount of NO₂ formed is ten times less than without dilution. In addition, for a global equivalence ratio equal to 1 for a dilution rate of 50%, there is no more oxygen to generate the formation of NO_x, the levels of NO and NO₂ are both reduced to 0 ppm. The maximum and minimum NO_x emissions for a gasoline engine are also plotted for an easier comparison with a current gasoline engine as already presented for other conditions [22]. Interestingly, the NO_x yielding is below the maximal value emitted by gasoline engines and falls below the minimum for a global equivalence ratio of 0.9 at a dilution of 50%. Such a result is very promising for the development of a technology using metal as energy carrier.

The Mg particle burns in a micro-flame to produce MgO which recondenses. The temperature of the MgO particles after recondensation – measured with the pyrometer - ranges between 1550 °C for a dilution of 50% to 2200 °C without any dilution [25]. It is not significantly influenced by the mass flow rate of magnesium and decreases when the dilution ratio increases. The observed temperature is below the theoretical value of 3000 K - which is close to the adiabatic flame temperature - obtained by Shoshin et al. [27] and Lim et al. [28]. Such a difference can be explained by the radiation and the convection heat losses in the combustion chamber that decrease the average flame temperature.

The mean residence time of the gas in the combustion chamber is approximately equal to 0.5 s. For such a duration, a significant amount of thermal NO_x can be produced only if the gas temperature is higher than 2000 K [25]. Such an assumption is well supported by a model based on the Zeldovich mechanism [29] and the associated kinetic parameters [30]. The duration of Mg oxidation is approximately equal to few milliseconds [31,32]. Hence NO_x formation occurs surely after Mg combustion is completed. It may occur in the gas phase in close contact with the surface of MgO particles where the gas temperature is higher than the mean gas temperature ranging from 800 °C to 1400 °C [23,25].

With such a global mechanism for NO_x formation, one can easily understand why the NO_x yielding increases when increasing the Mg mass flow rate. The total contact area between MgO surface and the gas increases as MgO concentration rises. The temperature of the particles decreases when the dilution factor increases. This could be explained by the depletion of oxygen in the flame when increasing the dilution ratio. For the highest equivalence ratio, the NO_x emission decreases due to the depletion of the available oxygen. The amount of oxygen becomes a limiting factor, causing a decrease in NO_x emission.

2.2.4. Characterization of the condensed phase-products and trapping

The particle filtration is challenging for such a combustion system. On one hand, the particle emissions standards have to be complied. On the other hand, all the metal oxides particles produced must be trapped inside the system for an optimal circular economy. Indeed, the yield of metal regenerated using renewable energy will depend on the metal oxide trapping efficiency.

TEM images of MgO samples collected in the combustion chamber show aggregates of particles (see Fig. 7). Cubic crystals of MgO of sizes ranging from 10 nm to around 1 μm are observed in agreement with the theory on magnesium oxide crystallization [33]. The cubic shape is in agreement with previous observations by [9] and [23]. The size of the aggregate of cubic crystals ranges from 200 nm to 1 μm. Considering the crystals interface, the transparency indicates mostly weakly agglomerated particles with very few crystallized links between them. Micron-sized agglomerates are formed probably after the deposition of MgO crystals on the walls of the combustion chamber and cyclone with some electrostatic or sintering effects as observed by SEM [23]. This

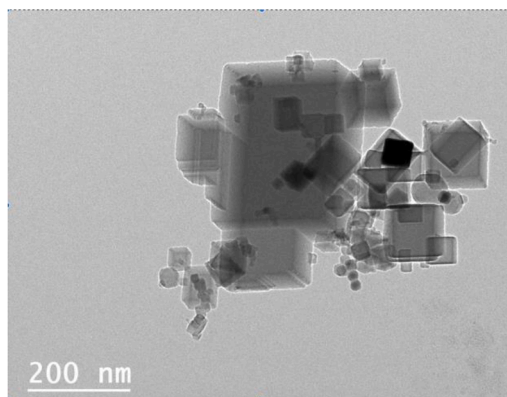


Fig. 7. TEM photographs of MgO particles (collected in the combustion chamber). Scale bar: 200 nm.

effect seems to be at the origin of the uniformization of the size distribution of the agglomerated particles from the combustion chamber to the secondary heat exchanger as proposed by [23].

With the combustion system equipped with two sets of cone/cyclone, the deposits of MgO particles are collected in the different parts of the system except in the secondary heat exchanger and in the exhaust line. It allows evaluating the mass fractions of MgO collected on the burner head, in the combustion chamber, in the cyclones and in the elbow, respectively. The mass distribution obtained for $S_g=0.7$ and an equivalence ratio of 0.63 is $4 \pm 0.3\%$ in the burner head, $35\% \pm 0.7\%$ in the combustion chamber, $11 \pm 0.4\%$ in cone 1, $31 \pm 1.1\%$ in cyclone 1, $3 \pm 0.1\%$ in cone 2 and $6 \pm 0.5\%$ in cyclone 2, respectively. The overall mass balance is not obtained as MgO is not collected in the heat exchanger and the exhaust line. For the samples collected at the chamber outflow, the combustion efficiency is near 100%, whatever the tested experimental conditions. There is no unburnt Mg at the chamber exit. Laraqui et al. [23] show that a global trapping efficiency of 98% on average is achieved when collecting the MgO in the overall system for an equivalence ratio of 0.39 and a swirl number equal to 0.8. These results indicate that the global mass trapping efficiency should not be a limiting parameter for a circular fuel cycle. However, the MgO trapping system needs to be improved considering the air emission standards.

2.3. Burner in ICARE (Aluminum)

2.3.1. Description of the facility

The solution adopted for this study uses a Bunsen-type burner in order to obtain a laminar, conical Al/air flame, evolving in a free field as illustrated in Fig. 8.

This experimental configuration also makes it possible to master and control the generating conditions allowing the stabilization of the metallic flame. The flow of each gaseous compound feeding the test bench is controlled by a Bronkhorst digital flow meter. The mean velocity profile extracted at the burner exit is flat with an average value of 1.3 m/s. The powder mass flow rate can be varied leading to equivalence ratios ranging from 0.8 to 1.5. For the suspension of the aluminum particles, the dispersion system chosen for the experimental bench is a Palas BEG 1000 commercial aerosol generator. An Ohaus Explorer digital recording balance, whose precision and response time are respectively 0.1 g and 1 s, was installed under the aerosol generator in order to temporally quantify the mass of dispersed powder. During the operation of the dispersion system, the mass flow of aluminum powder is then generally constant at the outlet of the generator and the latter has a very good repeatability.

The metal powder used for this work comes from industrial production. The Al ULTE 0665 range supplied by Poudres Hermillon specifies a high purity of aluminum and an average Sauter particle diameter of approximately 7.1 μm. The morphology and size

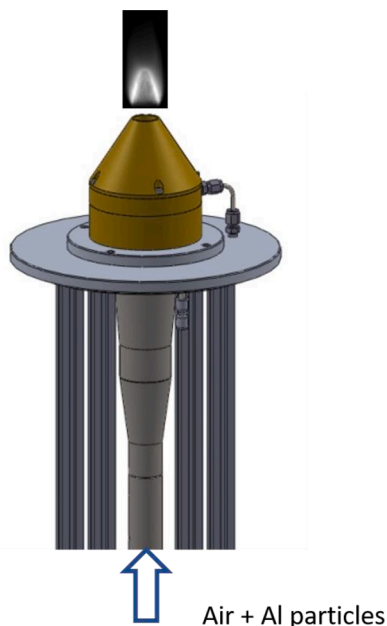


Fig. 8. Sketch of the Bunsen burner with the metal/air flame stabilized at the exit.

distribution of this powder in its initial state were analyzed with a Scanning Electron Microscope (SEM). Fig. 9 presents an example of SEM images obtained through secondary electrons. This aluminum powder is then mainly made up of spherical particles, without any particular agglomeration. Despite a dispersion observed in the size of the particles, the order of magnitude of the average diameter of the initial powder agrees with the value indicated by the manufacturer.

In order to comply with the health and safety standards of the laboratory, as well as to approach the concept of a metallic energy vector, a complementary system for the extraction and filtration of burnt gases was designed and installed above the experimental device. The chosen solution consists of a class H13 HEPA filter that can operate up to a continuous temperature of 300 °C.

Combustion is monitored by direct visualization thanks to a low-frequency camera (10 Hz, spatial resolution 20.9 pixels/mm, exposure time 10 μ s) equipped with a band-pass filter (F2, central wavelength 488 nm, FWHM 6 nm), highlighting the spatial distribution of the AlO(g) reaction intermediary and illustrating the flame geometry (see Fig. 10).

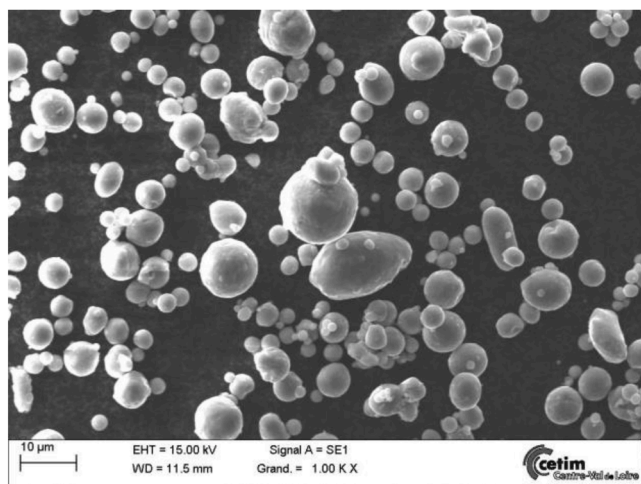


Fig. 9. Secondary-electron SEM image of the aluminum powder. Scale bar: 10 μ m.

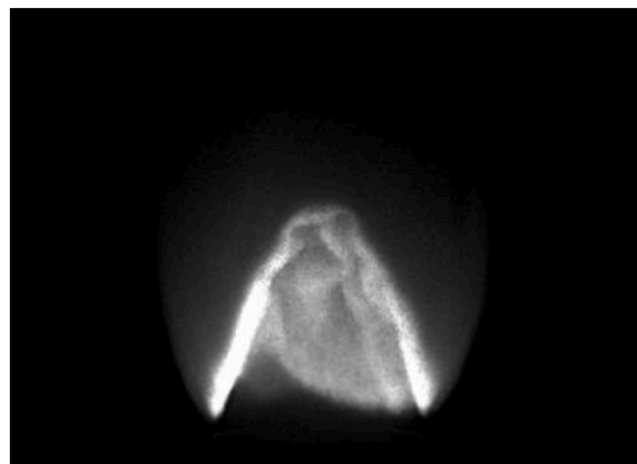


Fig. 10. Instantaneous image of the conical flame through the bandwidth of the main AlO(g) emission (i.e. at 488 nm). Burner exit diameter: 32 mm.

In addition, an optical fiber (diameter 200 μ m) and a spectrometer (Ocean Optics HR4000, linear CCD array) allows local spectral detection of the Al/air flame and a temperature determination using the emission of the AlO(g) reaction intermediate. The study of the flame/plume radiation was performed with a tangential gradient radiometer having a viewing angle of 150° and operating at wavelengths between 0.3 μ m and 20 μ m. This differential sensor measures only the radiated power per unit area by subtracting the convective flux from the total value.

Finally, the solid combustion products were sampled at different heights in the plume. These samples were then analyzed by transmission electron microscopy (TEM) and SEM coupled to an EDS probe to obtain compositional and morphological information on the combustion products.

2.3.2. Flame stabilization and reactivity

2.3.2.1. Laminar flame speed. The combustion of aluminum in the form of a cloud of particles is a multi-physical and complex process. The macroscopic analysis of the structure of the Al/air flame makes it possible to estimate its laminar propagation speed and could improve the understanding of the phenomenon of oxidation at the scale of a particle during a group combustion. For premixed flames, the thermal gradient between the exothermic reaction zone and the fresh gasses induces heat transport to the oxidizer/fuel mixture and, consequently, the propagation of combustion. The laminar flame velocity then defines the speed of the combustion wave at which it passes through the fresh gasses in the direction normal to the flame front [34]. With the use of a Bunsen-type burner, the premixed flame is stabilized thanks to the balance of speeds between the spread of the flame and the fresh gas component normal to the combustion front.

In previous work on this experimental device, the laminar flame velocity was initially estimated using the Al/air flame surface and mass conservation. Subsequently, the particle imaging velocimetry measurement technique was used and allowed a more accurate assessment of the laminar flame speed. With the powders used (average diameter of 7.1 μ m), a flame speed of about 35 cm/s was obtained for dust concentrations between $0.8 < \text{Equivalence Ratio} < 1.5$.

An instantaneous LASER tomography image is illustrated in Fig. 11 (a). It makes it possible to identify the condensed species, namely the aluminum powder in the fresh gasses and the alumina particles in the burnt gasses. A darker zone can be observed at the interface (conical zone) which corresponds to the reaction zone and to the evaporation of the aluminum particles, thus confirming that the particles mainly burn in the gaseous phase. The determination of the displacement of the particles between two successive images makes it possible to obtain

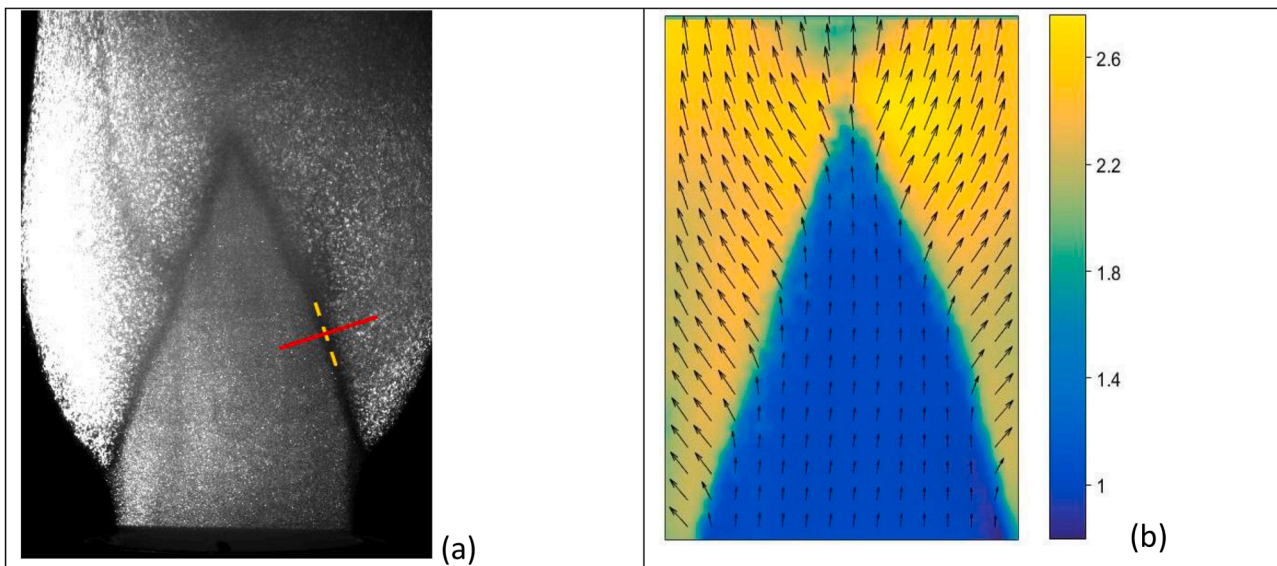


Fig. 11. (a): instantaneous LASER tomography image – (b): average velocity field of the condensed particles. Burner exit diameter: 32 mm. Adapted from [35].

instantaneous velocity fields, which can finally be averaged to lead to an average velocity field of the condensed particles as presented in Fig. 11 (b).

2.3.2.2. Spectroscopy for species identification and gas phase temperature measurement. A dimensionless emission spectrum of the reaction zone can be acquired using a spectrometer. This spectrum is composed of both a continuous background emission due to the thermal radiation of the condensed phase (mainly alumina particles at high temperature) and the emission of gaseous species. $\text{AlO}(\text{g})$ emissions (blue-green) are predominant as illustrated in Fig. 12.

The gas temperature can be determined by fitting the $\text{AlO}(\text{g})$ bands as detailed in [35]. A temperature around 3150 K was obtained for Al/air equivalence ratios ranging from 0.6 to 1.3. The presence of $\text{AlO}(\text{g})$ and $\text{Al}(\text{g})$ emissions, such as the magnitude of the gas phase temperature suggest that particles burn mainly in diffusion mode.

2.3.2.3. Heat balance. The study of the total radiation emitted by the flame was carried out using radiant power measurements perpendicular to the burner axis. The method of determining the total radiant power is the same as for traditional burner flames [21], consisting of integrating the axial profile on an imaginary cylindrical surface. The total radiant

power obtained by this method for a flame with 0.95 Al/air equivalence was $Pe = 5.9 \pm 0.5$ kW, corresponding to 78% of the estimated total power release of 7.6 kW, calculated assuming a full oxidation of the injected aluminum. The latest assumption was checked analyzing the composition of condensed combustion products. This extraordinary radiative fraction stems from the very high temperatures (3150 K) of the reaction zone. This result is clearly a sizing parameter for the design of future systems based on this technology.

2.3.3. Characterization of the condensed-phase products

The study of condensed combustion products makes it possible to validate the general mechanism of aluminum oxidation. For an equivalence ratio of 0.95, the condensed combustion products were collected by agglomeration on a metal rod in the plume 90 mm above the burner outlet, assuming all particle sizes have the same sticking ability. This sample was analyzed by electron microscopy. Although some micrometric spherical particles with diameters between 1 μm and 7 μm are found, the vast majority of the combustion products consist of nanometric particles. The sphericity of the larger particles indicates that they are formed in the liquid state during the combustion process, and they probably correspond to the molten alumina lobe residue present in the larger particles during vapor phase combustion. The amount of micrometric combustion products is in accordance with the initial alumina volume of the passive layer covering the largest aluminum particles.

Nanoscale products are spherical and follow a log-normal size distribution with a mode at a radius of 65 nm. EDS analyses of the nanometric products show that they are only composed of alumina.

The nanometric oxide particles (<100 nm) present a strong propensity to agglomerate. They were easily captured in different filtration systems such as cyclones and H13 high-efficiency particulate filters (EN1822-1:2009 / ISO29463-1). Although not quantified, it was clear from the fouling observed after the filtration systems that the HEPA filter efficiency is significantly higher. This kind of filter, even if they induce a significant pressure drop, should be favored. Importantly, nanoparticles were observed to be independent and an ethanol bath during sample preparation is sufficient to separate them.

Filtration of all the particles produced will be essential for the deployment of these vectors. In addition to the sanitary aspect which is obvious, it must also be remembered that the recovered oxides must then be regenerated. The work carried out at the LGRE has shown very good filtration levels but it is necessary to continue the work on this particular point. A solution would also be to modify the settings (oxidant

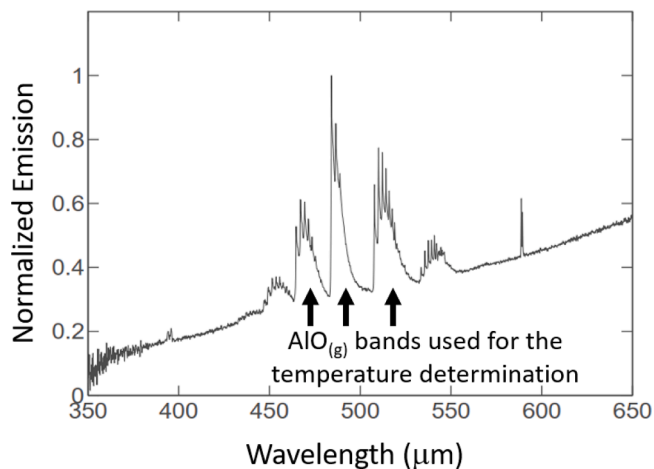


Fig. 12. Dimensionless emission spectrum for an equivalence ratio of 1.3, evidencing the vapor-phase nature of this combustion process.

mixture, pressure) in order to burn the particles in heterogeneous combustion mode. This would in fact make it possible to generate micrometric oxides that are easier to filter.

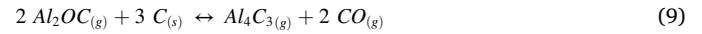
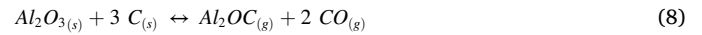
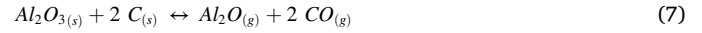
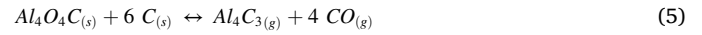
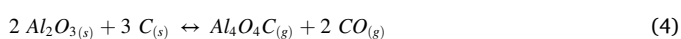
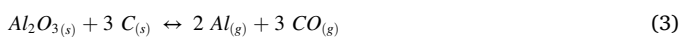
3. Solar carbo-thermal reduction

3.1. Objectives

As mentioned in the introduction, the regeneration of the metal fuels using CSP, through the reduction of the oxide produced by the combustion, makes the cycle more economically and environmentally beneficial and promotes the use of those fuels in future long-distance transportation. The reduction process is usually assisted with a reducing agent allowing to decrease the heat required for the reaction [36]. Ideally, methane is considered the best reducing agent; however, from an economic and environmental perspective, carbon is a better choice, particularly when provided by renewable sources such as charcoals. Moreover, the use of carbon becomes necessary, when using CSP as a heat source for the reduction process, to increase the solar absorptivity of the oxide powders. Balomenos et al. [37] proved that the production of aluminum is preferable through the carbothermal reduction process rather than the conventional Hall-Héroult process, even when the heat is provided from non-renewable sources (hydroelectric powered plant for both processes). From an energetic aspect, the carbo-reduction process supplies an exergy efficiency of 50%, 10% higher than the Hall-Héroult process. From an environmental aspect, the total CO₂-equivalent emissions for the carbo-reduction process are 2.4 kg/kg_{Al-produced}, lower than that for the Hall-Héroult process (3.8 kg/kg_{Al-produced}) [38]. Indeed, aluminum cannot be considered an alternative energy-carrying fuel when produced using the conventional Bayer/Hall-Héroult production process as the storage cycle efficiency is limited to 43% [39]. Furthermore, aluminum fuels are less efficient and more polluting than hydrogen and gasoline when produced through conventional methods [40].

A further decrease of the required heat for the carbo-thermal reduction process is possible when operating under low-pressure conditions, as validated by thermodynamic studies [41]. However, the use of vacuum is advantageous only if CSP is used to provide the heat of the reaction. For example, during alumina reduction using an electric-arc furnace (EAF), around 1.1 kg_{coal}/kg_{Al} is needed to provide heat at atmospheric pressure, while this value increases to 1.4 kg_{coal}/kg_{Al} at 1000 Pa (0.9 for heating and 0.5 for pumping power). Nevertheless, when using CSP, this value drops back to 0.5 kg_{coal}/kg_{Al} at 1000 Pa (only necessary for pumping power), making thus the use of CSP more attractive [37].

Further, the reaction mechanisms and kinetics are mainly determined by the operating pressure. Reactions (1) and (3) are the primary reactions occurring during the carbo-thermal reduction of magnesia and alumina respectively, however various secondary reactions may also take place. Under low vacuum conditions, meaning low CO partial pressure, the reaction kinetics of the magnesia reduction follows the solid-solid phase-boundary reaction (1) while the gas-phase diffusion reaction (2) is limited [42]. Thus, the C/MgO properties must be controlled to prevent the MgO sintering and to improve the reduction extent. Similarly, during alumina reduction, the formation of undesired Al-oxycarbide by-products from secondary reactions (4)-(9) can be limited, or even prevented, when operating under low pressure conditions (low CO partial pressure) [43].



Additionally, operating under low vacuum conditions is advantageous allowing to limit the reverse re-oxidation reaction and to produce highly pure metal powders. Indeed, Yang et al. [44] proved that both the temperature and pressure of the metal vapors determine the growth rate, purity and morphology of the produced metal powders. Thus, low pressures (P_{CO} < 10 Pa) and deposit temperature (730–870 K) are mandatory to prevent the reverse re-oxidation of the produced metal fuels [45].

Besides the economic and environmental aspects, the use of CSP as a heat source for the carbo-thermal reduction of oxides is favorable as it allows reaching high temperatures at very high heating rates (up to 500 K s⁻¹). This fast preheating is essential to reach the onset temperature of the reaction and thus reduce the magnesia sintering and the formation of unwanted Al-oxycarbide by-products.

Therefore, we are interested in developing a vacuum-assisted solar carbo-thermal reduction process for the regeneration of metal fuels from magnesia and alumina. The prospective use of metal fuels as transport fuels is directly dependent on the efficiency of the oxidation/reduction cycle and thus on the yields (y_{Mg} and y_{Al}) and purity (%Mg and %Al) of the produced metal fuels. The metal yields can be determined according to Eqs. (10) and (11) for magnesia and alumina respectively.

$$y_{\text{Mg}}(\%) = 100 m_{\text{Mg}} \% \text{Mg} / m_{\text{Mg}_{\text{gmax}}} \quad (10)$$

where $m_{\text{Mg}_{\text{gmax}}} = m_{\text{MgO}_{\text{initial}}} M_{\text{Mg}} / M_{\text{MgO}}$

$$y_{\text{Al}}(\%) = 100 m_{\text{Al}} \% \text{Al} / m_{\text{Al}_{\text{max}}} \quad (11)$$

where $m_{\text{Al}_{\text{max}}} = 2 m_{\text{Al}_2\text{O}_{3\text{initial}}} M_{\text{Al}} / M_{\text{Al}_2\text{O}_3}$

3.2. Process description

The developed solar process, shown in Fig. 13, consists of a solar-tracking heliostat, a parabolic concentrator and the Sol@rmet reactor. This 1.5-kW solar furnace allows concentrating the solar radiation up to 15 000 suns for direct normal irradiation (DNI) of 900–1000 W m⁻². Reduction experiments were performed even in batch mode or in semi-continuous mode. C/oxide powders Molar ratio (C/MgO = 1.25 and C/Al₂O₃ = 3) were milled together using different charcoal reducing agents and then pressed at dry to form pellets. The C/oxide ratios were obtained from previous investigations [46,47]. Those values are necessary to improve the reduction yield and sufficient in a way to keep the process energetically beneficial. For example, considering the use of charcoal (having an energy density of 0.09 kWh/mol) as a reducing agent with those ratios, the energetic gain is 0.08 kWh/mol Mg produced and 0.105 kWh/mol Al produced. The reduction occurs under argon carrier gas and a dry pump is used to apply the low vacuum. This pump has a constant pumping rate of 15 m³ h⁻¹, so the reaction pressure is adjusted by controlling the argon flow rate. One C/oxide pellet was placed on the graphite sample-holder at the focus of the parabola during the batch mode, while during the semi-continuous mode, several pellets were placed in an elevator system allowing to push them gradually to the focus of the parabola. Additionally, during the semi-continuous processing, an argon knife blower was added (see Fig. 13) to prevent the condensation of the produced metal powders on the glass dome. If so, this will cause the blockage of the solar radiation and the overheating of the glass dome. An optical monochromatic pyrometer was used to measure the temperature at the surface of the C/oxide pellet. A shutter,

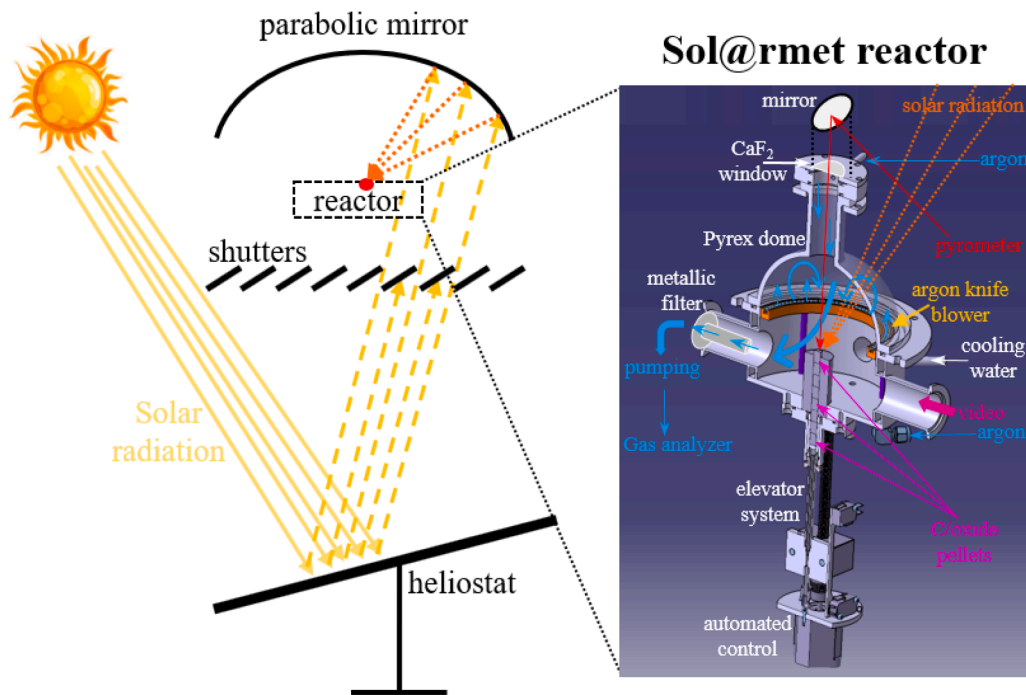


Fig. 13. Solar semi-continuous process for the regeneration of metal fuels through the carbo-thermal reduction of oxides. Adapted from [48].

placed between the heliostat and the parabola, allows controlling the passage of the direct solar radiation and thus the reaction heating and temperature along the reduction period. The produced metal powders were mainly collected on a porous stainless-steel filter (98%, 0.2 μm) placed at the exit of the Sol@rmet reactor and also on its metallic walls. Gaseous products (CO and CO₂) were sent to an infrared gas analyzer allowing to follow the reaction kinetics along the reduction period. The collected powders were then analyzed by XRD (X-Ray Diffraction) to determine their purity, by granulometry to determine their size and by SEM (Scanning Electron Microscopy) to determine their morphology and structure.

3.3. Batch solar experiments

3.3.1. Magnesia reduction

The first set of experiments was performed using commercial magnesia aiming to optimize the operating conditions and the C/MgO properties. We validated experimentally the numerical simulations proving that a swirl circulation can be created in the Sol@rmet reactor under low pressures (around 830 Pa) by controlling the gas flow rates and entries, that allows purging the produced metal powders and promotes the reduction [49]. Besides, a progressive increase of the temperature, along with the reaction, allows reducing the MgO sintering and dispersing of the CO emissions, thus improving the reaction extent [48]. Furthermore, we tested various charcoal reducing agents (commercial or synthesized) showing the effect of the pyrolysis conditions (biomass drying, maximal temperature, heating rate...). We produced charcoals with refined chemical (fixed carbon content, ash content...) and structural (porosity, specific surface area...) properties favoring thus the reduction yield. The biomass source is also important as wood-based, starch-based and cellulose-based charcoals performed better than sugar-based, mushroom-based and okara-based charcoals [50]. The effect of using metallic catalysts (Fe, Ni, Fe-Ni) was adverse as it accelerates the carbon consumption at the beginning of the reaction thus promoting magnesia sintering. Eventually, we reached a 96% yield of highly pure (96%) Mg powders by reducing the C/MgO particle size and contact through mechanical milling and the use of a bentonite binder. Most of the powders (more than 85%) were collected on the

metallic filter, while the remaining were collected on the metallic walls of the reactor and were less pure (60% Mg - 40% MgO). The produced Mg fuel powders consist of agglomerates of particles and crystals, having a D₉₀ size of $\sim 100 \mu\text{m}$, with a fine MgO layer [51].

The second set of experiments was performed using magnesia powders that were recovered from the combustion of magnesium fuels (performed at LGRE-UHA laboratory). The purity of those powders varies from extremely pure (full combustion, 100% MgO) to highly pure (93% MgO - 7% Mg) depending on the collection positions (combustion chamber or cyclone), the air to fuel ratio (AFR) and the exhaust gas recirculation (EGR) rate. In any case, similar results were attained, as when using commercial magnesia, with up to 91% Mg yield. However, we observed that, as previously, the powders collected on the metallic filter (about 85% of the total) were highly pure (96% Mg), while those condensed on the metallic walls of the Sol@rmet reactor were less pure (50–60% Mg) and remarkably contained about 10% of magnesium carbonate MgCO₃. This can be attributed to the existence of a small amount of unburned Mg, contained in the non-commercial magnesia powders, that may have promoted the reaction of magnesia with the produced CO and CO₂ gasses [52]. Fig. 14 shows the progress of the reaction kinetics in terms of CO and CO₂ production as a function of the temperature (controlled by the gradual opening of the shutters). It can be seen that, at 830 Pa, the reduction is almost complete in about 10 min for temperatures above 2100 K.

3.3.2. Alumina reduction

The first set of experiments was performed using commercial alumina (325 mesh) and proved the advantageous effect of the progressive heating as it will extend the CO emission along the reaction period and thus the reduction extent. Similarly, as for magnesia, the mechanical milling improves the contact between C/Al₂O₃ particles and reduces the particles size thus enhancing the reduction yield. Adding bentonite binder or metal catalysts boosts the formation of undesired Al₂O₃ carbide by-products at the beginning of the reaction and consequently is undesired. More importantly, we proved that the formation of those by-products can be limited, or even prevented, by operating under low pressures [53]. For example, no Al₄O₄C were detected at 830 Pa and decreasing the pressure to around 280 Pa increases the yield by around

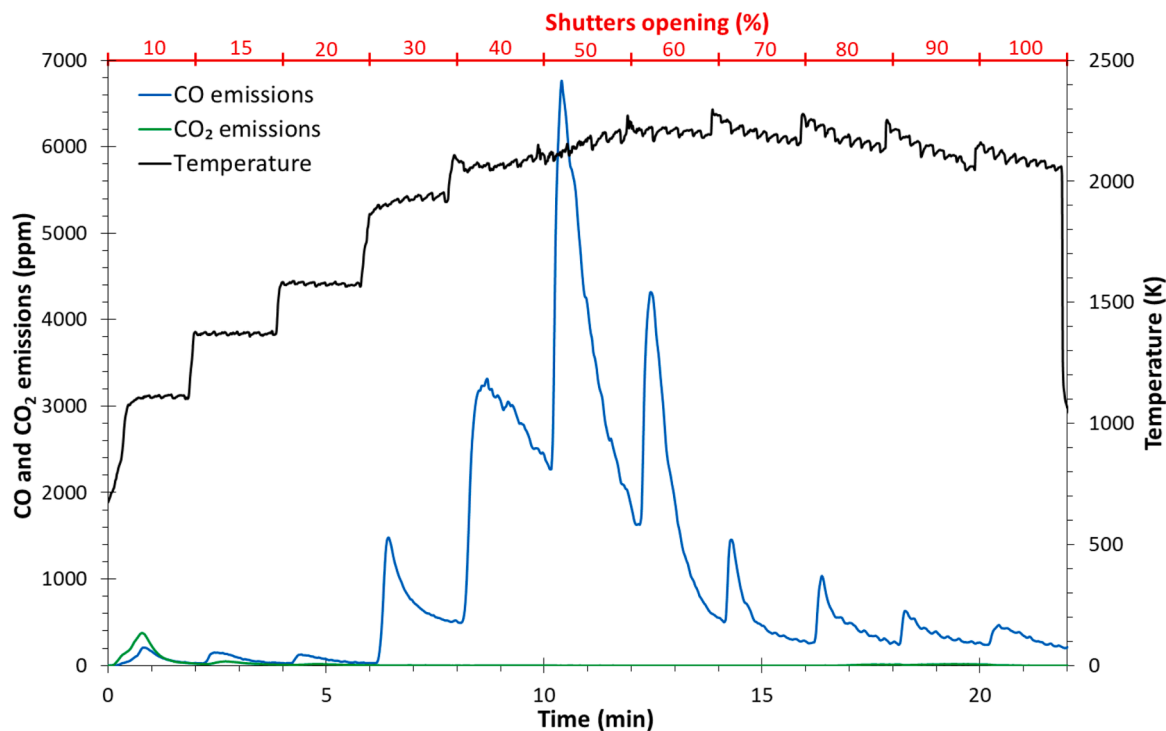


Fig. 14. Gaseous emissions and temperature as a function of the reduction time.

5%, reaching up to 77% Al yield. At this pressure, the formation of Al_2OC by-product was prevented and the purity of the produced powders was improved (91% instead of 84%). The produced powders consist of agglomerates of nano- and micro-sized Al particles (91% Al - 6% Al_4C_3 - 3% Al_2O_3) with a D_{90} size of 3 μm . We have also tried 100–200 mesh alumina to produce bigger Al agglomerates to limit their oxidation and carbonization, however, we obtained similar results. At the end of the reduction, the non-reacted remaining of the C/ Al_2O_3 pellet consisted mainly of carbon, $\text{Al}_3\text{O}_{3.5}\text{C}_{0.5}$, Al_4C_3 , Al_2OC , Al_xO_y , Al_2O_3 and some traces of Al (< 1%).

The second set of experiments was performed using alumina powders that were recovered from the combustion of aluminum fuels (performed at ICARE-CNRS laboratory). Notably, using those powders, the C/ Al_2O_3 pellet exploded directly as soon as it is subjected to the concentrated solar radiation when the shutter is barely opened (10% opening). As previously mentioned, CSP allows obtaining high heating rates thus attaining, in less than a second, around 800 K at 10% shutter opening. The explosion of the pellet was attributed to the structural composition of alumina as XRD measurements revealed the existence of γ - (20%), θ - (44%), δ - (13%) and α - Al_2O_3 (16%) unlike the previously used commercial α - Al_2O_3 . Indeed, those phases are less stable and can expand, in volume, when heated to transform into the α -phase. We attempted to pre-treat the alumina powders, through calcination in an electric tubular furnace, to convert those phases into α - Al_2O_3 . However, we obtained 80% θ - and 20% α - Al_2O_3 as we were limited by the maximal temperature of the furnace (1400 K). C/ Al_2O_3 pellet formed using those powders also exploded when subjected to the concentrated solar radiation. Besides the alumina phases, XRD also disclosed the existence of around 7% of unburned Al metal fuel that can incite the reaction and provoke the explosion of the pellet. Nevertheless, as the calcined powders (where the contained Al is oxidized) also exploded, we can attribute the explosion to the alumina phases rather than the existence of some metallic Al. As a solution, we were obligated to control very finely and slowly the shutter opening (open gradually 1% every 12 s to reach 10% after around 2 min). Similar reduction results were obtained as those using commercial alumina with a little improvement (82% Al yield) associated with the existence of some unburned Al (7%) that can catalyze the reduction.

3.4. Semi-continuous solar experiments

Semi-continuous solar experiments were performed using commercial magnesia and several problems were encountered along the reduction of the C/MgO pellets. The major issue was the condensation of the produced Mg metals on the glass dome thus blocking the solar radiation and provoking its overheating. This phenomenon could not be prevented under 4.5 L min^{-1} argon flow (allowing to operate at 830 Pa), even when adding an argon knife blower (see Fig. 13), as metals still condensed on some spots of the glass dome. So, to prohibit that, we were compelled to increase the flow to 10 L min^{-1} and consequently the pressure to 1240 Pa, thus limiting the reduction extent. Another issue was the melting of the C/MgO pellets on the surrounding graphite sample-holder (see Fig. 13) thus blocking the elevation system. So, we were forced to speed up the elevation that restrained the reaction time and thus the reduction efficiency. Nonetheless, despite those restrictions, a Mg yield up to 80% was attained.

4. General conclusions and perspectives

The STELLAR project described in this paper aims to provide a clear assessment of the potential of metallic particles as fuels, in terms of emissions, energy cost of production / recycling and energy requirements and autonomy of motor vehicles. To achieve this project, two different energy systems have been set up to produce heat from the combustion of micrometric metal particles. Two metals were selected for this study: magnesium and aluminum. It appears from these two studies that the durable stabilization of this type of flame requires a good control of the suspension of the particles. Almost all of the injected particles burn with the air. A very large part (>50%) of the energy is radiated from the reaction zone to the surrounding medium. This property, which results from the very high temperatures involved, will directly determine the heat recovery unit to be used. The oxides produced are heavier and bulkier than the initial particles, which complicates their post-combustion storage in on-board energy systems. Their filtration remains quite easy, despite their nanometric size, due to their strong propensity to agglomerate. Almost complete filtration is achievable with

conventional filtration systems. The formation of nitrogen oxides is favoured by high temperatures and an excess of oxygen. One solution to limit their concentration at the exhaust is to work close to stoichiometry. This does not impact the stabilization of the flame (the flame speed is not very dependent on the concentration of particles) nor the maximum temperatures reached around each individual particle. On the other hand, the medium being optically dense, the concentration as well as the characteristic dimension of the burner notably influence the radiative transfers within the flow.

Considering the regeneration of those metal fuels, we proved their efficient sustainable recycling using a solar process for the carbothermal reduction of the metal oxides produced from the combustion. Important metal yields, up to 96% Mg and 77% Al, of highly pure metal powders were obtained using commercial oxides. Similar results were obtained during the regeneration of the combustion oxide products. We were able to achieve these values by understanding the reduction kinetics (solid-solid or gas-solid phases, magnesia sintering, formation of Al-oxycarbide by-products), optimizing the reactor operating conditions (progressive heating, pressure, CO partial pressure, gas flow...) and improving the C/oxide properties (charcoal synthesis and properties, mechanical milling, C/oxide contact, bentonite binder). Furthermore, we developed a solar semi-continuous recycling process for which 80% Mg yield was reached despite the experimental restrictions. However, one must consider practical solutions for the condensation of the produced metal powders on the glass dome that causes its overheating.

Declaration of Competing Interest

The authors declare that they have no known competing financial interests or personal relationships that could have appeared to influence the work reported in this paper.

Data availability

Data will be made available on request.

Acknowledgments

Financial support from the French National Research Agency (convention ANR-18-CE05-0040) is gratefully acknowledged.

References

- [1] Fit for 55 - The EU's plan for a green transition, <https://europa.eu/17G9njr>; 2022 [accessed 11 october 2022].
- [2] Bergthorson JM. Recyclable metal fuels for clean and compact zero-carbon power. *Prog Energy Combust Sci* 2018;68:169–96. <https://doi.org/10.1016/j.pecs.2018.05.001>.
- [3] Markstein GH. Combustion of metals. *AIAA J* 1963;1:550–62. <https://doi.org/10.2514/3.1595>.
- [4] Bergthorson JM, Goroshin S, Soo MJ, Julien P, Palecka J, Frost DL, et al. Direct combustion of recyclable metal fuels for zero-carbon heat and power. *Appl Energy* 2015;160:368–82. <https://doi.org/10.1016/j.apenergy.2015.09.037>.
- [5] Loutzenhiser PG, Tuerk O, Steinfeld A. Production of Si by vacuum carbothermal reduction of SiO₂ using concentrated solar energy. *JOM* 2010;62:49–54. <https://doi.org/10.1007/s11837-010-0137-0>.
- [6] Lomba R, Halter F, Chauveau C, Bernard S, Gillard P, Mounaim-Rousselle C, et al. Experimental characterization of combustion regimes for micron-sized aluminum powders. In: 53rd AIAA Aerospace sciences meeting. American Institute of Aeronautics and Astronautics; 2015.
- [7] Garra P, Leysens G, Allgaier O, Schönnenbeck C, Tschamber V, Brilhac J-F, et al. Magnesium/air combustion at pilot scale and subsequent PM and NO_x emissions. *Appl Energy* 2017;189:578–87. <https://doi.org/10.1016/j.apenergy.2016.12.069>.
- [8] Dreizin EL. Metal-based reactive nanomaterials. *Prog Energy Combust Sci* 2009;35:141–67. <https://doi.org/10.1016/j.pecs.2008.09.001>.
- [9] Lomba R, Bernard S, Gillard P, Mounaim-Rousselle C, Halter F, Chauveau C, et al. Comparison of combustion characteristics of magnesium and aluminum powders. *Combust Sci Technol* 2016;188:1857–77. <https://doi.org/10.1080/00102202.2016.1211871>.
- [10] Gallier S, Braconnier A, Godfroy F, Halter F, Chauveau C. The role of thermophoresis on aluminum oxide lobe formation. *Combust Flame* 2021;228:142–53. <https://doi.org/10.1016/j.combustflame.2021.01.039>.
- [11] Braconnier A, Chauveau C, Halter F, Gallier S. Experimental investigation of the aluminum combustion in different O₂ oxidizing mixtures: effect of the diluent gases. *Exp Therm Fluid Sci* 2020;117:110110. <https://doi.org/10.1016/j.expthermflusc.2020.110110>.
- [12] Bazyn T, Krier H, Glumac N. Evidence for the transition from the diffusion-limit in aluminum particle combustion. *Proc Combust Inst* 2007;31:2021–8. <https://doi.org/10.1016/j.proci.2006.07.161>.
- [13] Bucher P, Yetter RA, Dryer FL, Vicenzi EP, Parr TP, Hanson-Parr DM. Condensed-phase species distributions about Al particles reacting in various oxidizers. *Combust Flame* 1999;117:351–61. [https://doi.org/10.1016/S0010-2180\(98\)00074-1](https://doi.org/10.1016/S0010-2180(98)00074-1).
- [14] Soo M, Mi X, Goroshin S, Higgins AJ, Bergthorson JM. Combustion of particles, agglomerates, and suspensions – a basic thermophysical analysis. *Combust Flame* 2018;192:384–400. <https://doi.org/10.1016/j.combustflame.2018.01.032>.
- [15] Yuasa S, Fukuchi A. Ignition and combustion of magnesium in carbon dioxide streams. *Symp (Int) Combust* 1994;25:1587–94. [https://doi.org/10.1016/S0082-0784\(06\)80804-0](https://doi.org/10.1016/S0082-0784(06)80804-0).
- [16] Corcoran AL, Hoffmann VK, Dreizin EL. Aluminum particle combustion in turbulent flames. *Combust Flame* 2013;160:718–24. <https://doi.org/10.1016/j.combustflame.2012.11.008>.
- [17] Law CK, Williams FA. Combustion of magnesium particles in oxygen-inert atmospheres. *Combust Flame* 1974;22:383–405. [https://doi.org/10.1016/0010-2180\(74\)90053-4](https://doi.org/10.1016/0010-2180(74)90053-4).
- [18] Wang S, Corcoran AL, Dreizin EL. Combustion of magnesium powders in products of an air/acetylene flame. *Combust Flame* 2015;162:1316–25. <https://doi.org/10.1016/j.combustflame.2014.10.016>.
- [19] Dreizin EL, Hoffmann VK. Constant pressure combustion of aerosol of coarse magnesium particles in microgravity. *Combust Flame* 1999;118:262–80. [https://doi.org/10.1016/S0010-2180\(98\)00144-8](https://doi.org/10.1016/S0010-2180(98)00144-8).
- [20] Legrand B, Marion M, Chauveau C, Gokalp I, Shafirovich E. Ignition and combustion of levitated magnesium and aluminum particles in carbon dioxide. *Combust Sci Technol* 2001;165:151–74. <https://doi.org/10.1080/00102200108935830>.
- [21] Dreizin EL, Berman CH, Vicenzi EP. Condensed-phase modifications in magnesium particle combustion in air. *Combust Flame* 2000;122:30–42. [https://doi.org/10.1016/S0010-2180\(00\)00101-2](https://doi.org/10.1016/S0010-2180(00)00101-2).
- [22] Laraqui D, Allgaier O, Schönnenbeck C, Leysens G, Brilhac J-F, Lomba R, et al. Experimental study of a confined premixed metal combustor: metal flame stabilization dynamics and nitrogen oxides production. *Proc Combust Inst* 2019;37:3175–84. <https://doi.org/10.1016/j.proci.2018.07.018>.
- [23] Laraqui D, Leysens G, Schönnenbeck C, Allgaier O, Lomba R, Dumand C, et al. Heat recovery and metal oxide particles trapping in a power generation system using a swirl-stabilized metal-air burner. *Appl Energy* 2020;264:114691. <https://doi.org/10.1016/j.apenergy.2020.114691>.
- [24] Feikema D, Chen R-H, Driscoll JF. Enhancement of flame blowout limits by the use of swirl. *Combust Flame* 1990;80:183–95. [https://doi.org/10.1016/0010-2180\(90\)90126-C](https://doi.org/10.1016/0010-2180(90)90126-C).
- [25] Andrieu A, Allgaier O, Leysens G, Schönnenbeck C, Brilhac J-F. NO_x emissions in a swirled-stabilized magnesium flame. *Fuel* 2022;321:124011. <https://doi.org/10.1016/j.fuel.2022.124011>.
- [26] Maiboom A, Tauzia X, Hétet JF. Influence of high rates of supplemental cooled EGR on NO_x and PM emissions of an automotive HSDI diesel engine using an LP EGR loop. *Int J Energy Res* 2008;32:1383–98. <https://doi.org/10.1002/er.1455>.
- [27] Shoshin Y, Dreizin E. Particle combustion rates in premixed flames of polydisperse metal–Air aerosols. *Combust Flame* 2003;133:275–87. [https://doi.org/10.1016/S0010-2180\(02\)00571-0](https://doi.org/10.1016/S0010-2180(02)00571-0).
- [28] Lim J, Lee S, Yoon W. A comparative study of the ignition and burning characteristics of afterburning aluminum and magnesium particles. *J Mech Sci Technol* 2014;28:4291–300. <https://doi.org/10.1007/s12206-014-0943-3>.
- [29] Zeldovich Y, Frank-Kamenetskii D, Sadovnikov P. *Oxidation of nitrogen in combustion*. Publishing House of the Acad of Sciences of USSR; 1947.
- [30] Hanson RK, Salimian S. Survey of rate constants in the N/H/O system. editor. In: Gardiner WC, editor. *Combustion chemistry*. New York, NY: Springer New York; 1984. p. 361–421.
- [31] Cassel HM, Liebman I. Combustion of magnesium particles I. *Combust Flame* 1962;6:153–6. [https://doi.org/10.1016/0010-2180\(62\)90084-6](https://doi.org/10.1016/0010-2180(62)90084-6).
- [32] Shevtsov VI, Fursov VP, Stesik LN. Mechanism for combustion of isolated magnesium particles. *Combust Explo Shock Waves* 1976;12:758–63. <https://doi.org/10.1007/BF00740747>.
- [33] Geysersmans P, Finocchi F, Goniakowski J, Hacquart R, Jupille J. Combination of (100), (110) and (111) facets in MgO crystals shapes from dry to wet environment. *Phys Chem Chem Phys* 2009;11:2228–33. <https://doi.org/10.1039/B812376D>.
- [34] Glassman I, Yetter R. *Combustion*. 4th ed. San Diego, USA: Elsevier Inc.; 2008.
- [35] Lomba R, Laboureur P, Dumand C, Chauveau C, Halter F. Determination of aluminum-air burning velocities using PIV and Laser sheet tomography. *Proc Combust Inst* 2019;37:3143–50. <https://doi.org/10.1016/j.proci.2018.07.013>.
- [36] Steinfeld A, Kuhn P, Tamaura Y. CH₄-utilization and CO₂-mitigation in the metallurgical industry via solar thermochemistry. *Energy Convers Manage* 1996;37:3127–3132. [https://doi.org/10.1016/0196-8904\(95\)00341-X](https://doi.org/10.1016/0196-8904(95)00341-X).
- [37] Balomenos E, Panias D, Paspaliaris I, Friedrich B, Jaroni B, Steinfeld A, et al. Carbothermic reduction of alumina: a review of developed processes and novel concepts. In: *Proceedings of EMC*; 2011. p. 729–43.

- [38] Balomenos E, Panias D, Paspaliaris I. Exergy analysis of metal oxide carbothermic reduction under vacuum–sustainability prospects. *Int J Thermodyn* 2012;15: 141–8. <https://dergipark.org.tr/en/pub/ijot/issue/5785/76897>.
- [39] Shkolnikov EI, Zhuk AZ, Vlaskin MS. Aluminum as energy carrier: feasibility analysis and current technologies overview. *Renew Sustainable Energy Rev* 2011; 15:4611–23. <https://doi.org/10.1016/j.rser.2011.07.091>.
- [40] Utgikar VP, Lattin W, Jacobsen RT. Nanometallic fuels for transportation: a well-to-wheels analysis. *Int J Energy Res* 2007;31:99–108. <https://doi.org/10.1002/er.1255>.
- [41] Puig J, Balat-Pichelin M. Production of metallic nanopowders (Mg, Al) by solar carbothermal reduction of their oxides at low pressure. *J Magnesium Alloys* 2016; 4:140–50. <https://doi.org/10.1016/j.jma.2016.05.003>.
- [42] Xiong N, Tian Y, Yang B, B-q Xu, Dai T, Y-n Dai. Results of recent investigations of magnesia carbothermal reduction in vacuum. *Vacuum* 2019;160:213–25. <https://doi.org/10.1016/j.vacuum.2018.11.007>.
- [43] Puig J, Balat-Pichelin M. Experimental carbothermal reduction of Al₂O₃ at low pressure using concentrated solar energy. *J Sustain Metall* 2020;6:161–73. <https://doi.org/10.1007/s40831-020-00266-7>.
- [44] Yang C-b, Tian Y, Qu T, Yang B, Xu B-q, Dai Y-n. Analysis of the behavior of magnesium and CO vapor in the carbothermic reduction of magnesia in a vacuum. *J Magnesium Alloys* 2014;2:50–8. <https://doi.org/10.1016/j.jma.2014.02.003>.
- [45] Vishnevetsky I. Solar thermal reduction of metal oxides as a promising way of converting CSP into clean electricity on demand. In: *Proceedings of solar world congress*; 2015.
- [46] Puig J, Balat-Pichelin M. Experimental carbothermal reduction of MgO at low pressure using concentrated solar energy. *J Min Metall Sect B-Metall* 2017;54: 39–50. <https://doi.org/10.2298/JMMB170215048P>.
- [47] Halmann M, Frei A, Steinfeld A. Vacuum carbothermic reduction of Al₂O₃, BeO, MgO-CaO, TiO₂, ZrO₂, HfO₂ + ZrO₂, SiO₂, SiO₂ + Fe₂O₃, and GeO₂ to the metals. a thermodynamic study. *Miner Process Extr Metall Rev* 2011;32:247–66. <https://doi.org/10.1080/08827508.2010.530723>.
- [48] Berro Y, Puig J, Balat-Pichelin M. Improving the process of metallic fuels production through the solar carbothermal reduction of magnesia. In: 7th World congress on mechanical, chemical, and material engineering; 2021. <https://doi.org/10.11159/mmme21.102>. Prague (virtual), Czech Republic.
- [49] Berro Y, Masse R, Puig J, Balat-Pichelin M. Improving the solar carbothermal reduction of magnesia for metallic fuels production through reactor designing, milling and binders. *J Cleaner Prod* 2021;315:128142. <https://doi.org/10.1016/j.jclepro.2021.128142>.
- [50] Berro Y, Kehrli D, Brilhac J-F, Balat-Pichelin M. Metal fuel production through the solar carbothermal reduction of magnesia: effect of the reducing agent. *Sustain Energy Fuels* 2021;5:6315–27. <https://doi.org/10.1039/D1SE01549D>.
- [51] Berro Y, Puig J, Balat-Pichelin M. Improving the solar carbothermal reduction of magnesia as a production process of metal fuels. *Int J Min Mat Metall Eng* 2021;7: 22. <https://doi.org/10.11159/ijmmme.2021.003>.
- [52] Stopic S, Dertmann C, Modolo G, Kegler P, Neumeier S, Kremer D, et al. Synthesis of magnesium carbonate via carbonation under high pressure in an autoclave. *Metals (Basel)* 2018;8:993. <https://doi.org/10.3390/met8120993>.
- [53] Berro Y, Balat-Pichelin M. Metal fuels production for future long-distance transportation through the carbothermal reduction of MgO and Al₂O₃: a review of the solar processes. *Energy Convers Manage* 2022;251:114951. <https://doi.org/10.1016/j.enconman.2021.114951>.